Effect of relaxation on the oxygen *K*-edge electron energy-loss near-edge structure in yttria-stabilized zirconia

S. Ostanin,[1,2] A. J. Craven,[1] D. W. McComb,[2] D. Vlachos[1,2], A. Alavi,[3,*] M. W. Finnis,[3] and A. T. Paxton[3]
[1]*Department of Physics and Astronomy, University of Glasgow, Glasgow G12 8QQ, Scotland, United Kingdom*
[2]*Department of Chemistry, University of Glasgow, Glasgow G12 8QQ, Scotland, United Kingdom*
[3]*Atomistic Simulation Group, School of Mathematics and Physics, Queen's University, Belfast BT7 1NN, United Kingdom*
(Received 31 May 2000)

The electron energy-loss near-edge structure (ELNES) at the oxygen *K*-edge has been investigated in a range of yttria-stabilized zirconia (YSZ) materials. The electronic structure of the three polymorphs of pure ZrO_2 and of the doped YSZ structure close to the 33 mol % Y_2O_3 composition have been calculated using a full-potential linear muffin-tin orbital method (NFP-LMTO) as well as a pseudopotential based technique. Calculations of the ELNES dipole transition matrix elements in the framework of the NFP-LMTO scheme and inclusion of core hole screening within Slater's transition state theory enable the ELNES to be computed. Good agreement between the experimental and calculated ELNES is obtained for pure monoclinic ZrO_2. The agreement is less good with the ideal tetragonal and cubic structures. This is because the inclusion of defects is essential in the calculation of the YSZ ELNES. If the model used contains ordered defects such as vacancies and metal Y planes, agreement between the calculated and experimental O *K*-edges is significantly improved. The calculations show how the five different O environments of $Zr_2Y_2O_7$ are connected with the features observed in the experimental spectra and demonstrate clearly the power of using ELNES to probe the stabilization mechanism in doped metal oxides.

I. INTRODUCTION

Yttria-stabilized zirconia (YSZ) has been the subject of many experimental and theoretical studies due to the commercial applications of zirconia-based materials.[1,2] YSZ is formed by the addition of Y_2O_3 to ZrO_2 and results in the stabilization of the tetragonal or cubic phase depending on the molar fraction of Y_2O_3. While Y_2O_3 is probably the most widely used, stabilization using other binary oxides such as CaO, MgO, and La_2O_3 is also possible.

Pure ZrO_2 exhibits three well-defined polymorphs at ambient pressure: the monoclinic (*m*) phase which is stable up to about 1170 °C, the tetragonal (*t*) phase which is stable up to 2370 °C, and, finally, the cubic (*c*) phase that exists up to the melting point of 2680 °C. It has been reported that *m* phase transforms to an orthorhombic structure at high pressure.[3] The Zr^{4+} ion in *m*-ZrO_2 is found in seven fold co ordination with the O^{2-} ions, while in the *t* phase the Zr^{4+} ion is located in distorted eight fold coordination environments. The high-temperature *c* phase has the fluorite (CaF_2) structure with each metal ion in regular eightfold coordination sites with all of the Zr-O bonds of equal length.

Yttria has a large solid solubility range in ZrO_2 and hence can be used to stabilize both the *t* and *c* phases. It is interesting to note that the $t \rightarrow m$ transformation temperature of $(ZrO_2)_{1-x}(Y_2O_3)_x$ decreases significantly with increase in Y_2O_3 content *x*. In practice, the *t* and *c* phases can be retained for an indefinite time in a metastable state at low temperature over the composition range ($t, 0.02 < x < 0.09$, and $c, 0.04 < x < 0.4$). For $x > 0.4$, $Zr_3Y_4O_{12}$, an ordered rhombohedral phase, is reported to form.[4]

In YSZ the trivalent dopant cations Y^{3+} substitute for some of the Zr^{4+} ions and, in order to maintain charge neutrality, assuming formal ionic charges, one O vacancy must be created for each pair of dopant cations. The presence of O vacancies in YSZ reduces the average cation coordination number from 8, as in pure *t*- or *c*-ZrO_2, to a value between 7 and 8 depending on the dopant concentration. Though the exact nature of the atomic displacements in YSZ remains unclear, one can suppose that the relaxation of the ions away from their regular lattice sites results in local coordination environments that are similar to those found in *m*-ZrO_2. Recent x-ray and neutron diffraction experiments suggest that the YSZ *c* phase contains ''locally ordered regions of vacancies and dopants.''[5] It was reported that at low ($x < 0.15$) concentrations of Y_2O_3 there are regions ~ 15–20 Å in size which contain (i) isolated O vacancies and (ii) O vacancies arranged in pairs on nearest-neighbor anion sites in the [111] fluorite direction, with the cation site located between them occupied by a Zr^{4+} ion.[5] The O vacancies cause the tetragonal lattice distortions observed clearly at $x < 0.09$. Goff and co-workers[5] suggested that another type of defect cluster formed as the *x* increases: the [111] vacancy pairs pack together as in the $Zr_3Y_4O_{12}$ structural motif to form aggregates whose size and number increase slightly with *x*. The number of the isolated vacancies also increases with *x*. It is thought that these isolated vacancy atomic clusters become mobile at $T > 1000$ K, resulting in a rise of the ionic conductivity of YSZ. Since the anion-deficient YSZ crystal structure, with its dependence on dopant concentration and temperature, has a complex nature, a confirmation of the above interpretation[5] from further experiments and theoretical modeling is desirable.

To date, no full quantitative description of the stabilization mechanism of YSZ has been reported. Extended x-ray absorption fine structure (EXAFS) can distinguish between

the host and dopant cations, allowing the individual coordination polyhedra to be probed. However, EXAFS studies published to date are somewhat contradictory: several studies have concluded that an Y ion is nearest neighbor (NN) to the vacancy (for example, Ref. 6) while others have reported that yttrium occupies next-nearest neighbor (NNN) cation sites.[7] These inconsistencies are partly due to experiments being performed on samples with different dopant concentrations leading to different displacements of the regular fluorite lattice sites near to the vacancies.

Electron-energy-loss spectroscopy (EELS), via analysis of the energy-loss near-edge structure (ELNES), has developed into a powerful technique for the investigation of the unoccupied electronic states of crystals. This is especially true when the technique is carried out in a modern analytical electron microscope as this enables information to be obtained with high spatial resolution. ELNES results when the energetic incoming electron excites a core level electron into an empty state above the Fermi level (E_F). Analysis of the energy lost by the fast electron provides information about the unoccupied density of states (DOS). Due to the localized nature of the excitation process and the fact that a dipole selection rule is active, the DOS information is both site and symmetry projected. Hence it is possible to compare directly the experimental ELNES data with the results of density functional theory calculations. This approach has been used in the past by many authors utilizing a number of different reciprocal-space[8–10] and real-space[11] band structure methods. The calculation is complicated by the core hole produced during the excitation process. This influences the ELNES spectrum by distorting the local DOS in the vicinity of the excited atom and means that the correspondance between the calculated angular-momentum-projected DOS and ELNES intensity is not exact. There are a few models that attempt to take this core hole effect into account. The most widely used is the $Z+1$ approximation,[12] where the core hole is simulated as an increase in the effective nuclear charge at the excited site. Another model, used recently by Lie and co-workers,[13] proposes omission of one of the core shell electrons and the corresponding addition of one electron to the valence band. It has been shown recently that use of Slater's transition-state approximation results in improved agreement between the theoretical and experimental EELS threshold energy.[14] Within this model half of a core hole is retained in order to account for the screening effects that are absent in the one electron approximation. In the present paper, we investigate the use of the O *K*-edge ELNES to probe the electronic structure of YSZ and attempt to calculate, with Slater's transition-state theory, the observed ELNES using a structural model that includes both dopant atoms and an O vacancy.

The paper is organized as follows. In Sec. II we describe briefly the experimental methods used. The theoretical techniques have been described in detail elsewhere[14] and Sec. III includes our theoretical results for the relaxation and band structure of pure ZrO_2 and YSZ. In Sec. IV we discuss the results of our calculated O *K*-edge ELNES of the defective and defect-free zirconias and compare these with our ELNES measurements. In conclusion, we summarize the ability of our model to interpret the experimental data.

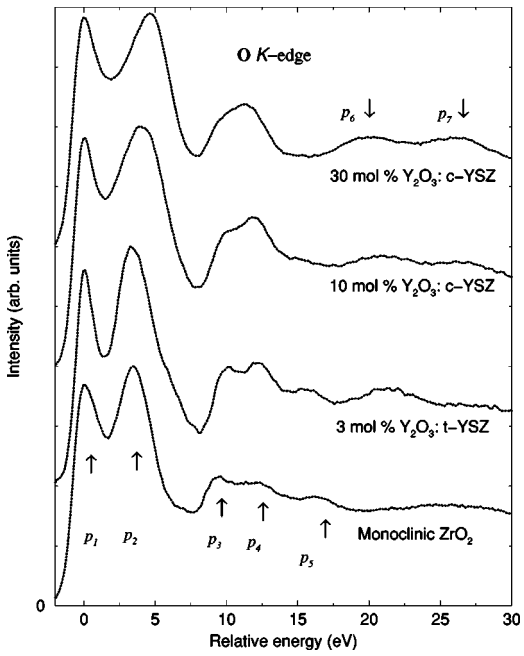

FIG. 1. The experimental O *K*-edge ELNES from *m*-ZrO_2 and YSZ samples.

II. EXPERIMENT

This section provides a brief summary of the experimental method. The zirconia and YSZ materials were supplied by MEL Chemicals. Samples were initially characterized using powder x-ray diffraction to check phase purity and by electron microscopy to measure grain size, the Y/Zr composition ratio, and homogeneity.

The ELNES investigations were carried out using a 100 kV VG HB5 dedicated scanning transmission electron microscope (STEM) with post-specimen lenses and equipped with a GATAN 666 PEELS spectrometer. A convergence semi angle of 11 mrad was used, giving a probe diameter of $\sim$1 nm and a probe current of $\sim$0.2 nA. The collection semi-angle used was 12.5 mrad. A background of the form AE^{-r} was removed from the O *K*-edge spectra, the low-loss spectrum was to used to deconvolute the plural scattering, and the spectra were then sharpened by deconvoluting the detector point spread function.[15] The spectra from a number grains of material were checked for consistency and then summed. Hence the data are averaged over a range of orientations.

The processed ELNES spectra for *m*-ZrO_2, 3 mol %(*t*-), 10mol %(*c*-), and 30 mol %(*c*-) Y_2O_3-ZrO_2 are displayed in Fig. 1. For comparison purposes the energy of the first peak p_1 in each spectrum has been set to zero energy. Two peaks p_1 and p_2 are clearly observed in the energy region close to the threshold energy of the edge. It is clear that the depth of the minimum between these two peaks changes as the Y_2O_3 concentration increases. Specifically, the minimum is much deeper in the *t* specimen than in either *m*- or *c*-YSZ. There is also a shift of the second peak p_2 to higher energy as the Y_2O_3 concentration increases. The next minimum in the ELNES (around 8 eV) is noticably wider in pure *m*-ZrO_2 than in any of the YSZ specimens. Farther from the threshold another pair of peaks is observed in the energy region between 8 and 15 eV. Although the splitting between these

peaks is not well resolved in pure ZrO_2, it is in the *t* sample. As the dopant concentration increases further the second peak p_4 in this energy region becomes dominant and the splitting becomes progressively more difficult to resolve. In the high-energy region ($E>15$ eV), a very weak feature p_5 is observed in *m*-ZrO_2 and *t*-YSZ but it appears to be absent in the cubic specimens. A pair of weak peaks p_6 and p_7 are observed between 20 and 25 eV in *c*-YSZ. As the dopant concentration decreases the first one p_6 moves up in energy and closer to p_7. The p_6 feature is still present in *t*-YSZ but is absent or very weak in *m*-ZrO_2. Note that the observed O *K*-edge ELNES spectra for YSZ are in agreement with previous measurements.[16]

III. BAND STRUCTURE CALCULATIONS

A. Computational methods

In order to model pure ZrO_2 and the defect YSZ system, we have used a combination of two first-principles density functional theory (DFT) methods in the local density approximation. For energy minimization with respect to lattice constants and local atomic displacement we employ the plane-wave, pseudopotential-based free energy molecular dymanics (FEMD) technique.[17] It is generally accepted that this is the most efficient scheme for precise calculation of total energy and force. The plane-wave method is less effective for electronic structure calculations where one looks for the fine detail in reciprocal space. Moreover the details of the core wave functions are lost. Therefore, for the calculation of the densities of states and dipole matrix elements [Eq. (1) below] we use the atomic positions generated by the FEMD in an all-electron linear muffin-tin orbital (NFP-LMTO) method.[18] The latter also employs an analytic force theorem. As we will demonstrate, the structure generated by FEMD is also in equilibrium with respect to the LMTO forces. In fact as we shall see, for structural energy differences the two methods are in almost perfect agreement. The computational details of the NFP-LMTO method used for band structure calculation of pure ZrO_2 have been described previously.[19,20]

Let us outline briefly some details of the FEMD calculations. The Troullier-Martins pseudopotentials[21] are used for O, Zr, and Y atoms. For Zr and Y, pseudopotentials are constructed for the semicore $4s$ and $4p$ atomic states rather than the $5s$ and $5p$ valence states. A rather high cutoff energy of 75 Ry for the plane-wave representation of Kohn-Sham orbitals was used and integration over the Brillouin zone (BZ) was performed using the special Monkhorst-Pack mesh.

The simplified approach[22] to ELNES within the pseudopotential band structure technique neglects the energy dependence of the matrix elements, significantly restricting its ability to interpret the experimental data in the case of YSZ. Conversely, all-electron DFT methods are easily extended to calculate one-electron dipole matrix elements exactly.[10,14] Furthermore, one can partly account for many-electron effects within Slater's transition-state theory.[14] A further benefit of the all-electron NFP-LMTO method[18] is that the core states are allowed to relax when solving the Kohn-Sham DFT equations self-consistently.

B. Pure zirconia

Several *ab initio* calculations have been published recently for bulk phases of pure ZrO_2.[19,20,23–25] In studying the structural stability, the main theoretical efforts have been concentrated on obtaining the accurate zero temperature DFT energies within the local density and/or generalized gradient approximation. The energy vs volume curves calculated recently give a reasonable agreement (see, for example, Ref. 19) with experimental results.

The sequence of ZrO_2 structural transformations, $m \rightarrow t \rightarrow c$, with temperature may be determined by comparing the free energies of different phases. The cubic *c* phase of ZrO_2 has one degree of freedom, its unit cell volume, the *t* phase has two additional degrees: the axial c/a ratio and the symmetry breaking displacement of O atoms, δ. The displacements of O atoms lead to half of the Zr-O bonds becoming stronger and the other half weaker compared with the bonds in ideal *c* phase. By calculating the c/a unit cell deformation and atomic δ displacements in the *t* phase Jansen[26] and Jomard *et al.*[24] showed that *c* structure is unstable against the internal δ O displacements along the *z* direction. The height of this instability barrier depends strongly on the volume and the exchange-correlation potential used. A complete analysis of the ZrO_2 $c \rightarrow t$ transition in terms of the Landau theory has been done by Fabris and co-workers[20] who used the polarizable self-consistent tight-binding model.[19] It has been shown[27,20] that the $c \rightarrow t$ transformation is displacive of the second order and is driven by the softening of the X_2^- phonon mode. As for the $m \rightarrow t$ transition, no microscopic mechanism for its initiation has been proposed up to now. Some interesting theoretical predictions concerning the surface energies and relaxation of *t* and *m*-ZrO_2 have been made recently.[28]

Calculation of the three ambient-pressure phases of ZrO_2 as the testing benchmark is a starting point of our study. We use both the NFP-LMTO method[18] within the LDA and the FEMD technique[17] to relax the volume and atom positions. The structure parameters of ZrO_2 calculated by us together with the experimental data by Howard *et al.*[29] are collected in Table I. All data are given in terms of the 12-atom unit cell to make a comparison more transparent. There is excellent agreement between theory and the experimental data. Small differencies exist between the FEMD results and the previous pseudopotential calculations[23] within the same framework. These are due to using our numerical scheme to fit the equation of state[30] instead of the Murnaghan equation of state fitting.

The correct hierarchy $E^m < E^t < E^c$ in the energy vs volume of different ambient-pressure ZrO_2 phases is reproduced. In particular, the NFP-LMTO method gives energy differencies $\Delta E^{c-t} = 0.049$ eV/ZrO_2 and $\Delta E^{c-m} = 0.105$ eV/ZrO_2 while the FEMD code shows values 0.046 eV/ZrO_2 and 0.102 eV/ZrO_2, respectively. These data are in good agreement with experimental values[31] that are derived from enthalpy differencies at corresponding phase transition temperatures: $\Delta U^{c-t} = 0.057$ eV/ZrO_2 and $\Delta U^{c-m} = 0.12$eV/ZrO_2.

C. Simplified model of the defect structure of YSZ

1. Relaxation

To investigate the nature of O vacancies in cubic YSZ, we perform calculations by the FEMD method on an 11-atom

TABLE I. Calculated equilibrium lattice parameters of the *c*, *t*, and *m* phases of ZrO_2 referred to the 12-atom unit cell compared with the experimental data given in Ref. 29. Here δ denotes the internal degree of freedom of *t*-ZrO_2, β is the angle of the *m* cell, and *x*, *y*, *z* are the fractional coordinates of the three nonequivalent sites in the *m* phase.

		Expt.	NFP-LMTO	FEMD
c-ZrO_2	a(Å)	5.088	4.995	5.078
t-ZrO_2	a(Å)	5.048	5.009	5.030
	c/a	1.026	1.014	1.038
	δ/c	0.057	0.051	0.066
m-ZrO_2	a(Å)	5.149	4.982	5.126
	b/a	1.012	1.036	1.009
	c/a	1.032	1.057	1.048
	β	99.23	98.57	99.20
	x_{Zr}	0.275	0.274	0.274
	y_{Zr}	0.040	0.040	0.041
	z_{Zr}	0.208	0.212	0.210
	x_{O-1}	0.070	0.069	0.069
	y_{O-1}	0.332	0.339	0.338
	z_{O-1}	0.345	0.338	0.348
	x_{O-2}	0.450	0.448	0.449
	y_{O-2}	0.757	0.753	0.760
	z_{O-2}	0.479	0.478	0.481

supercell of seven O atoms, two Zr atoms, and two Y atoms, obtained by removing a single atom from the O sublattice of *c*-ZrO_2 and substituting two Zr atoms by two Y atoms. This $Zr_2Y_2O_7$ cell, shown in Fig. 2(a), contains two formula units of ZrO_2 and one formula unit of Y_2O_3 and corresponds to a composition of 33 mol%Y_2O_3. Note that our nonrelaxed cell exhibits an artificial layered cation structure having pure Zr $z=0$ and $z=1$ planes whereas the $z=\frac{1}{2}$ plane contains Y atoms only. We allow the internal coordinates to relax while keeping the lattice parameter at the experimental bulk value of $(ZrO_2)_{0.7}(Y_2O_3)_{0.3}$, namely, 5.2 Å. The number of the Monkhorst-Pack $\vec{k}$ points required to get an accurate relaxation within the FEMD method was investigated. The special $2\times2\times2$ Monkhorst-Pack grid in the Brillouin zone is adequate for both the total energy and atomic displacements.

The atomic relaxation can be described with reference to the position of the Zr atom at the origin of the cell in Fig. 2(a), as shown in Fig. 2(b). This illustrates the rather complex distortions that reduce the fcc symmetry of the metal sublattice. The calculated fractional coordinates of the relaxed atom positions relative to the Zr atom at the origin, are listed in Table II. In this description, the Zr-2 ions relax along [110] and the Y-1 and Y-2 ions relax along the directions close to [010] and [100], respectively. The anion sublattice relaxation is also illustrated in Fig. 2(b) and shows how the O atoms columns shift with respect to each other along [001]. These distortions are similar to the O displacements of *t*-ZrO_2. The O-O distances along the vacancy-free O columns show minor changes with respect to the nonrelaxed geometry while the O column with a defect has a double O-O distance. The particular displacements of the O atoms in the perfect columns along [001] (i.e., all sites except O-2) depend slightly on the distance from the vacancy site, with an average value of 0.187 Å. In the vacancy-containing column, the O atom on the O-2 site moves downward with a displacement of 0.98 Å. This is probably indicative of the high mobility of vacancies along the O columns.

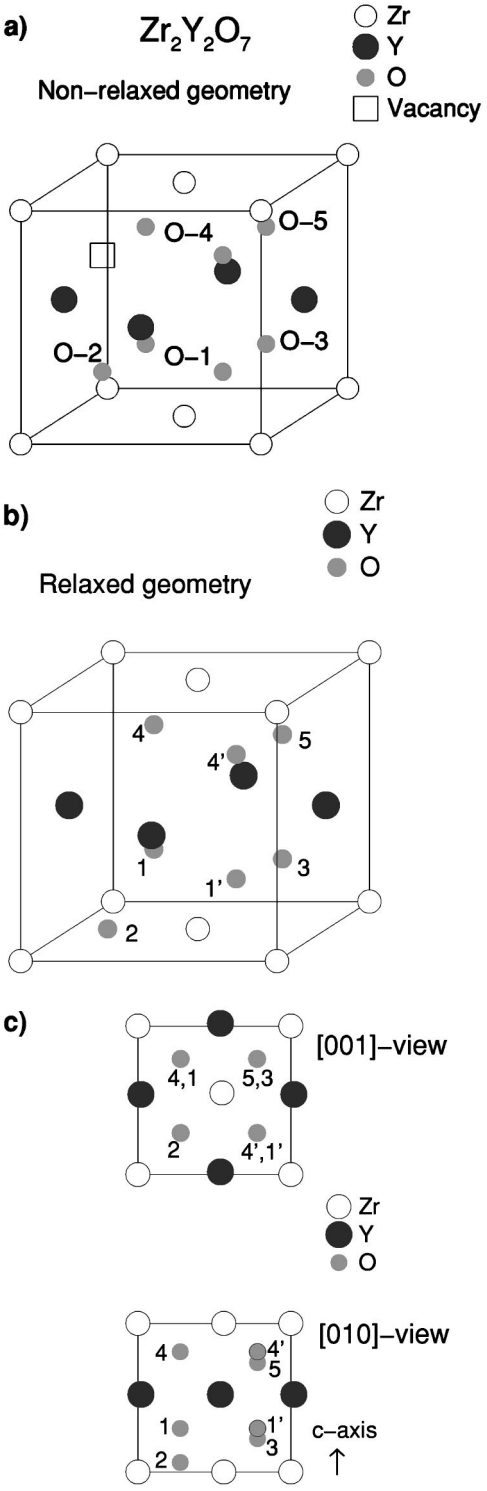

FIG. 2. Model of the $Zr_2Y_2O_7$ cell (a) with nonrelaxed geometry and (b) after relaxation. Two Zr atoms and two Y atoms form the nearest-neighbor shell to the vacancy. The five different types of O atoms, corresponding to the fractional coordinates given in Table II, are indicated. The plan views shown in (c) represent the views along the [001] and [010] directions.

TABLE II. Calculated fractional coordinates in the $Zr_2Y_2O_7$ cell after relaxation.

Site	*x*	*y*	*z*
Zr-1	0	0	0
Zr-2	0.554	0.554	0
Y-1	0.013	0.541	0.501
Y-2	0.541	0.013	0.501
O-1	0.277	0.782	0.291
O-1′	0.782	0.277	0.291
O-2	0.277	0.277	0.062
O-3	0.782	0.782	0.222
O-4	0.277	0.782	0.808
O-4′	0.782	0.277	0.808
O-5	0.782	0.782	0.734

Referring to Fig. 2(b), we see that the O-2 atom in the column containing the vacancy lies a little above the $z=0$ plane. This asymmetric arrangement is dictated by the fixed Zr positions at constant volume and introduces a double well into the potential energy surface, a symmetry-equivalent structure being that with the O-2 atom the same distance below the $z=0$ plane after allowing all other atoms to relax. It is probable that further relaxations would occur if the lattice constants were also allowed to relax. Note that after relaxation each Zr ion is sevenfold coordinated by oxygen ions as in *m*-ZrO_2.

After performing the relaxation of the $Zr_2Y_2O_7$ cell by means of the FEMD method, the relaxed coordinates were used in a further energy minimization using the total energy and forces with the NFP-LMTO method. Changes in atomic positions calculated in this way were smaller than 0.2% of the lattice parameter.

2. Density of states and band gap

It is well known that the LDA calculations underestimate[25] the fundamental band gap of ZrO_2 whereas the experimental gaps derived from vacuum ultraviolet spectroscopic measurements might be too high, with an uncertainty of about 1 eV. The observed minimum band gaps of *c*, *t*, and *m* phases reported by French *et al.*[32] are 6.7–7.08 eV, 5.78–6.62 eV, and 5.83–7.09 eV, respectively, while EELS gives band gaps of 4.6, 4.2, and 4.2 eV(Ref 16) for *c*-YSZ, *t*-YSZ, and *m*-ZrO_2, respectively. It should be noted that the experimental *t* and *c* samples compared were single or polycrystalline stabilized materials containing different Y_2O_3 concentrations. Previous band structure calculations within the LDA found a direct band gap in cubic ZrO_2 in the range 3.3-4.1 eV.[23,25,26] For pure ZrO_2, our NFP-LMTO DOS calculations give a band gap of 3.45 eV for *c*-ZrO_2 and a slightly larger gap of 3.6 eV for *m*-ZrO_2. The discrepancy with experiment with respect to the trend can be attributed to the fact that measurements for *c* and *t* structures were on samples stabilized by Y_2O_3. In YSZ the direct band gap has been estimated at around 5.2–5.8 eV from absorption and photoluminescence spectroscopy[33] while an apparent reduction due to an absorption tail has also been reported.[34]

Comparing the site-projected DOS of unrelaxed and relaxed $Zr_2Y_2O_7$ in Fig. 3, we see the importance of atomic

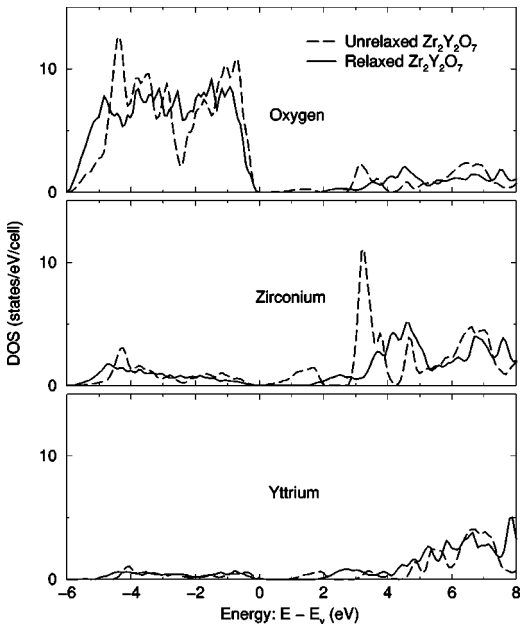

FIG. 3. Total site-projected DOS for $Zr_2Y_2O_7$ before and after relaxation. E_v is the top of valence band.

relaxation in YSZ. Whereas in the unrelaxed model there are midgap states, these are practically eliminated by relaxation as also found by Stapper *et al.*.[23] In our relaxed model these are reduced to conduction band tails. We do not know whether these tails would also be removed by further relaxing the lattice constants in our model cell. These matters are of importance in understanding the origin of color centers as well as predicting whether ZrO_2 may be *self-doped* by the intoduction of acceptor levels at vacancies.

The total and site- and Mulliken-projected DOS of $Zr_2Y_2O_7$ after relaxation are derived from the energy bands. The major features of the DOS can be summarized as follows. The upper valence band has a width of 6 eV and is formed mainly by the $2p$ states of the five types of O atoms while the $3d$ states of Zr and Y contribute to the DOS peak at around -5 eV. There is good agreement between the occupied O valence band of the defective ZrO_2 obtained in our calculations with the experimental valence-band photoemission spectra of French *et al.*[32] who report, for the *c* phase, a broad $O-2p$ band which extends from 0 to -7 eV binding energy. The conduction-band DOS of $Zr_2Y_2O_7$ is mainly composed of cation-projected *d* states in the range 2–10 eV. Above 11 eV, most of the significant structure in the DOS comes from the anion-projected *p* states.

The three panels of Fig. 4 compare the unoccupied O total DOS in pure *c*-ZrO_2, unrelaxed $Zr_2Y_2O_7$, and relaxed $Zr_2Y_2O_7$. The O DOS of $Zr_2Y_2O_7$ before relaxation shows the first pronounced peak at ~ 1.5 eV, just above the top of the valence band, E_v, and the second peak at ~ 3 eV. These two peaks, which lie in the fundamental band gap of pure *c*-ZrO_2, are separated by the gap of 0.8 eV associated with the e_g-t_{2g} DOS splitting in the ideal *c* structure. However, the relaxed geometry produces the O DOS which is similar to the corresponding DOS of pure *c*-ZrO_2, cleaning the DOS in the fundamental band gap between 0 and 2 eV and suppressing the DOS between 5.5 and 6.5 eV. In $Zr_2Y_2O_7$ there

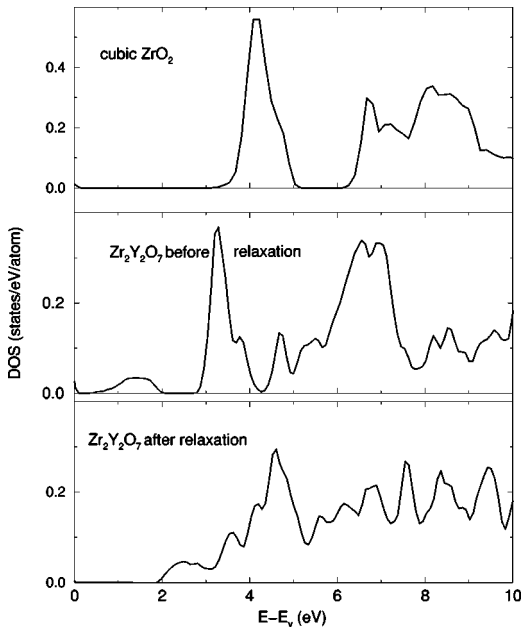

FIG. 4. The DOS of the O site in perfect c-ZrO_2 (top panel) as well as the O DOS of $Zr_2Y_2O_7$ cell with nonrelaxed (middle panel) and relaxed (bottom panel) geometry. The average O DOS of the five types of O atoms in $Zr_2Y_2O_7$ is plotted.

are five different types of O site, each of which exhibits a different DOS. In Fig. 4 we show the total DOS over all O sites but for ELNES purposes it is necessary to calculate the spectrum of each type of site.

IV. ELNES

A. Formalism

In EELS the intensity, or cross section, is measured as a function of the energy loss E in the inelastic scattering caused by excitation of an initial core state with energy ϵ_c and eigenfunction $\phi_c(\vec{r})$. The final band states with energies $\epsilon_{n\vec{k}}=\epsilon_c+E$ and eigenfunctions $\psi_{n\vec{k}}(\vec{r})$ which are involved in the EELS process can be calculated *ab initio* within the one-electron approximation. Using Fermi's golden rule[35] and therefore assuming the first Born approximation for scattering, one can define the EELS cross section σ in atomic units as follows:

$$\sigma(E)\propto\frac{1}{W_0}\sum_{n,\vec{k}}|<\psi_{n\vec{k}}|e^{i\vec{q}\cdot\vec{r}}|\phi_c>|^2\delta(E+\epsilon_c-\epsilon_{n\vec{k}}), \quad (1)$$

where W_0 is the energy of the incoming electron beam, and the dipole approximation $e^{i\vec{q}\cdot\vec{r}}\approx 1+(i\vec{q}\cdot\vec{r})$ is used further to calculate the matrix elements. Note that after making the dipole approximation the theories of ELNES and x-ray absorption near-edge structure (XANES) lead to similar expressions. Introducing a coordinate system such that $-z$ is parallel to the incident beam direction, the appropriate linear combination of x, y, and z components of the dipole matrix elements must be evaluated in the case of an anisotropic single crystal. If the experimental data are averaged over many crystal orientations, as here for YSZ, the average value of the x, y, and z components of the matrix elements is the appropriate linear combination to be calculated.

The most important consequence of the dipole approximation is that selection rules require that the final states must have angular momentum $l\pm 1$ if the core state has angular momentum l. As Muller *et al.*[9] have pointed out, expression (1) resembles a local DOS, like a Mulliken projection onto basis functions with certain angular momentum centered at a particular atomic site. Hence, the Mulliken-projected DOS can be used as a rather crude approach to identify peak positions[9,14] in the ELNES, but prediction of the peak intensities requires the inclusion of matrix elements.

We calculate the ELNES at the anion K edge including the dipole matrix elements with the LMTO method.[14] In order to allow a direct comparison of the calculated ELNES shape with experiment a broadening mechanism must be applied to take into account the initial- and final-state lifetime broadening as well as the instrumental resolution. The Lorentzian linewidth $\Gamma(E)=\Gamma_i+\Gamma_f$ is used where Γ_i is the width of the initial core states obtained from atomic data.[37] The Lorentzian linewidth for the final states Γ_f has the form[9,14]

$$\Gamma_f=\frac{\pi^2\sqrt{3}}{128}E_p\left(\frac{E-E_v}{E_v-E_0}\right)^2. \quad (2)$$

Here E_p is the plasmon energy which can be obtained from the low-loss region of the energy-loss spectrum, while E_v-E_0 is the width of the occupied part of the bands, which is defined here as the energy between the bottom of the O s band, E_0, and the top of the valence band, E_v. This assumption, i.e., Eq. (2), has been tested successfully for anion K-edge ELNES in transition-metal nitrides and carbides.[14] The theoretical spectra are finally convoluted with a 0.5 eV full width at half maximum (FWHM) Gaussian to account for the instrumental resolution.

If several types of excited atom are present in a unit cell, the matrix elements from each different site must be aligned to take account of the binding energy appropriate to the site and then combined as a weighted sum.

A short comment on how to calculate the threshold energy E_{th} within DFT should be made here. If the core-level energy $\epsilon_c(q_c)$ is linear in the number of electrons q_c occupying the core state, then according to Slater's transition-state theory,[36] $E_{th}=-\epsilon_c(q_c)\ |_{q_c=3/2}$. When the self-consistent all-electron LDA calculation within Slater's transition state theory is performed, allowing core-level relaxation, it gives E_{th} as the Fermi energy relative to the core level with half of a core hole. Such an approach, which has been applied already by Paxton and co-workers[14] to the transition-metal nitrides and carbides, is used here to calculate absolute values of the O K-edge threshold energies in ZrO_2.

B. Pure zirconia

The absolute energies of the O K-edge threshold calculated within Slater's transition-state theory for pure c- and t-ZrO_2 are 535.2 eV and 535.5 eV, respectively. There are two nonequivalent sites in m-ZrO_2. O-I has a calculated threshold of 535.8 eV and O-II has a threshold of 535.5 eV. These latter values for m-ZrO_2 compared with our experimental EELS E_{th} of 533.3 ± 0.26 eV show that Slater's

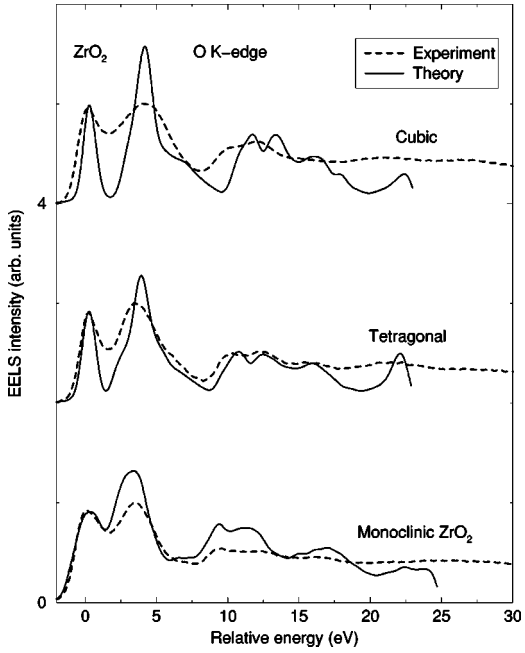

FIG. 5. Oxygen *K*-edge ELNES for *m*, *t* (3 mol %Y_2O_3-ZrO_2), and *c* (10 mol %Y_2O_3-ZrO_2) compared with calculation for pure, defect-free ZrO_2 in each phase.

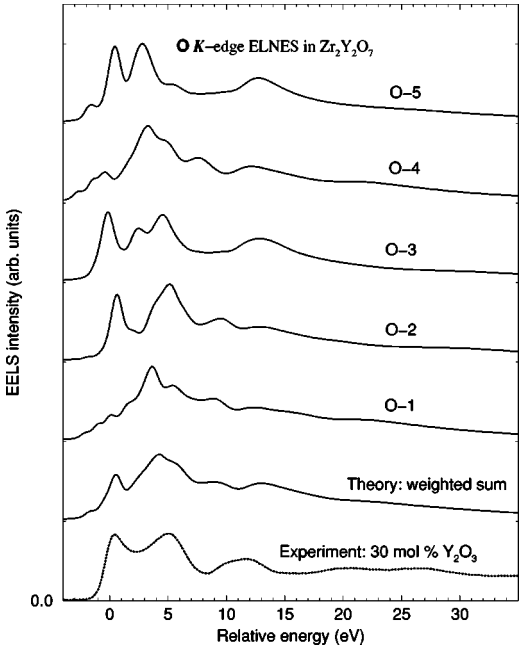

FIG. 6. Calculated O *K*-edge ELNES for each O site in $Zr_2Y_2O_7$. The weighted mean is compared with the experimental result for the 30 mol %Y_2O_3-ZrO_2 sample.

transition-state theory overbinds this core energy by ~ 2 eV. An overbinding of 4 eV for the *K*-edge E_{th} has been obtained recently applying the same approach to the transition metal carbides and nitrides.[14] Note that the one-electron approximation underbinds the core levels, giving, for example, 486.0 eV in the case of *m*-ZrO_2.

Figure 5 compares the calculated O *K*-edge shape for the perfect *m*, *t*, and *c* structures of ZrO_2 with the experimental ELNES from the corresponding stabilized structures. The 3% and 10% Y_2O_3 samples were chosen as closest to the pure *t*- and *c*-ZrO_2, respectively. The energy of the first peak p_1 has been defined as zero, and the experimental and calculated shapes have been aligned and intensity matched at this energy. In the calculation for *m*-ZrO_2, a weighted sum of O *K*-edge ELNES for both types of O sites has been made taking into account the threshold shift of 0.3 eV.

Taking *m*-ZrO_2 first, the calculation is done for the same structure as the material measured. There is excellent agreement with the peak positions up to 10 eV. Beyond that, the DFT calculation becomes unreliable. For *t*-ZrO_2, the main discrepancy between the predicted and observed shapes is in the region of the first two low-energy peaks p_1 and p_2. The predicted dip is much bigger and the width of p_2 is much smaller than observed. The agreement for *c*-ZrO_2 is even worse in this energy region and the features above 5 eV are not well predicted.

These findings are perhaps not surprising, as each unit of Y_2O_3 replaces two Zr atoms with Y atoms and introduces a vacancy on the O sublattice. In the 3 mol %(*t*-) and 10 mol %(*c*-)Y_2O_3-ZrO_2 specimens used to measure the ELNES, the presence of the dopant fills up the ELNES pseudogap between the p_1 and p_2 peaks and causes a gradual shift of the p_2 peak to higher energy. The next minimum ($5\ \text{eV} < E < 8\ \text{eV}$) also changes with the concentration of dopant and, consequently, with the crystallography. In particular, this observed minimum is wider in the *m* phase than in the other specimens. The depth and shape of this minimum are in fair agreement with our calculation in *m*-ZrO_2 but show gradually worsening agreement from the *t* to the *c* phase. The discrepancies in the *c* and *t* phases between the experimental and calculated ELNES shapes emphasize the need to include the dopants and vacancies in the model structure. However, a useful result of our calculations is the good prediction of the different distances between p_1 and p_2, which therefore suggests that this is a parameter which characterizes the YSZ structure.

C. YSZ

The predicted O *K*-edge ELNES shapes from the five different O sites of $Zr_2Y_2O_7$ after relaxation are shown in Fig. 6 along with their weighted mean and the O *K* edge from the measured ELNES of the 30 mol %Y_2O_3-ZrO_2 sample. The calculated shifts of the core level have been included. Good agreement is obtained between the calculated weighted average and the experimental shape in the low-energy region. The positions of the main peaks p_1 and p_2 are reproduced even though individual shapes from the five nonequivalent sites differ markedly. The noticeable discrepancy in the ELNES spectrum in the higher-binding-energy region (10–15 eV) can be attributed to the simplicity of our ordered tetragonal model for YSZ.

V. CONCLUSIONS

The reported features of the experimental shapes of the O *K*-edge ELNES depend on the crystal structures and the Y_2O_3 composition and provide us with further information to improve our understanding of YSZ.

Ab initio calculations were performed to obtain the O *K*-edge ELNES in pure and yttria-stabilized zirconia. The

benefits and limitations of this theoretical approach have been discussed. Good agreement between calculated and measured ELNES data was obtained for pure *m*-ZrO_2 with respect to the number of maxima, the intensity ratios, and energy positions of the peaks. Poor agreement between the experimental ELNES from 3 mol% and 10 mol% Y_2O_3-ZrO_2 and the calculated shapes for pure *t*- and *c*-ZrO_2, respectively, is attributed to the absence of defects in the unit cells of the pure materials.

A comparison of the experimental anion *K*-edge ELNES in 30 mol% Y_2O_3-ZrO_2 with the calculated shape from a vacancy-containing 11-atom cell, which models 33 mol% Y_2O_3-ZrO_2, yields very satisfactory results for the positions of the two main peaks. The discrepancy in the range 11–17 eV of binding energy is presumably due to the simplicity of our defect-ordered crystal cell. The reported findings suggest it will be worthwhile to carry out more realistic *ab initio* calculations of YSZ using larger unit cells. Currently, calculations for $(96-x)$-atom supercells of $(ZrO_2)_{32-2x}(Y_2O_3)_x$ are in progress.

In studying YSZ we have demonstrated that relaxation of defects plays an important role. Our calculations relate the detailed changes in the relaxed structure to the experimentally observed ELNES shapes and their variation with Y_2O_3 content. The combination of ELNES with detailed theoretical modelling shows great potential for the characterization of doped metal oxides.

ACKNOWLEDGMENTS

This work has been supported by the EPSRC under Grant Nos. L66963 and L66908, the European Science Foundation STRUC PSIK Network, MEL Chemicals, and Johnson Matthey.

*Present address: Department of Chemistry, University of Cambridge, Cambridge CB2 1EW, U.K.

[1] E.C. Subbarao, in *Science and Technology of Zirconia*, edited by A.H. Heuer and L.W. Hobbs, *Advances in Ceramics*, Vol. 3 (American Ceramic Society, Westerville, OH, 1981).
[2] R. Stevens, *Zirconia and Zirconia Ceramics*, Magnesium Electron Publication No. 113 (Magnesium Elektron Ltd., Manchester, UK, 1986).
[3] O. Ohtaka, T. Yamanaka, S. Kume, E. Ito, and A. Navrotsky, J. Am. Chem. Soc. **74**, 505 (1991).
[4] H.G. Scott, Acta Crystallogr., Sect. B: Struct. Crystallogr. Cryst. Chem. **33**, 281 (1977).
[5] J.P. Goff, W. Hayes, S. Hull, M.T. Hitchings, and K.N. Clausen, Phys. Rev. B **59**, 14 202 (1999).
[6] M.H. Tuilier, J. Dexpert-Ghys, H. Dexpert, and P. Lagarde, J. Solid State Chem. **69**, 153 (1987).
[7] P. Li, W. Chen, and J.E. Penner-Hahn, Phys. Rev. B **48**, 10 063 (1993); **48**, 10 082 (1993).
[8] J.E. Müller and J.W. Wilkins, Phys. Rev. B **29**, 4331 (1984).
[9] D.A. Muller, J. Singh, and J. Silcox, Phys. Rev. B **57**, 8181 (1998).
[10] M. Nelhiebel, P.-H. Louf, P. Schattschneider, P. Blaha, K. Schwarz, and B. Jouffrey, Phys. Rev. B **59**, 12 807 (1999).
[11] A.L. Ankudinov, B. Ravel, J.J. Rehr, and S.D. Conradson, Phys. Rev. B **58**, 7565 (1998).
[12] H.P. Hjalmanson, H. Büttner, and J.D. Dow, Phys. Rev. B **24**, 6010 (1981).
[13] K. Lie, R. Hoier, and R. Brydson, Phys. Rev. B **61**, 1786 (2000).
[14] A.T. Paxton, M. van Schilfgaarde, M. MacKenzie, and A.J. Craven, J. Phys.: Condens. Matter **12**, 729 (2000).
[15] A.J. Craven, J. Microsc. **180**, 250 (1995); A.J. Craven and L.A.J. Garvie, Microsc. Microanal. Microstruct. **6**, 89 (1995).
[16] D.W. McComb, Phys. Rev. B **54**, 7094 (1996).
[17] A. Alavi, J. Kohanoff, M. Parrinello, and D. Frenkel, Phys. Rev. Lett. **73**, 2599 (1994).
[18] M. Methfessel and M. van Schilfgaarde, *NFP Manual 1.01* (IHP, Frankfurt, 1997).
[19] M.W. Finnis, A.T. Paxton, M. Methfessel and M. van Schilfgaarde, Phys. Rev. Lett. **81**, 5149 (1998).
[20] S. Fabris, A.T. Paxton, and M.W. Finnis, Phys. Rev. B **61**, 6617 (2000).
[21] N. Troullier and J.L. Martins, Phys. Rev. B **43**, 1993 (1991).
[22] S. Köstlmeier and C. Elsässer, Phys. Rev. B **60**, 14 025 (2000).
[23] G. Stapper, M. Bernasconi, N. Nicoloso, and M. Parrinello, Phys. Rev. B **59**, 797 (1999).
[24] J. Jomard, T. Petit, L. Magaud, G. Kresse, and J. Hafner, Phys. Rev. B **59**, 4044 (1999).
[25] B. Kralik, E.K. Chang, and S.G. Louie, Phys. Rev. B **57**, 7027 (1998).
[26] H.J.F. Jansen, Phys. Rev. B **43**, 7267 (1991).
[27] K. Negita, Acta Metall. **37**, 313 (1989).
[28] A. Christensen and E.A. Carter, Phys. Rev. B **58**, 8050 (1998).
[29] C.J. Howard, R.J. Hill, and B.E. Reichert, Acta Crystallogr., Sect. B: Struct. Sci. **B44**, 116 (1988).
[30] S.A. Ostanin and V.Yu. Trubitsin, Phys. Rev. B **57**, 13 485 (1998).
[31] R. Ackermann, E.G. Rauh, and C.A. Alexander, High. Temp. Sci. **7**, 304 (1975).
[32] R.H. French, S.J. Glass, F.S. Ohuchi, Y.-N. Xu, and W.Y. Ching, Phys. Rev. B **49**, 5133 (1994).
[33] P. Camagni, P. Galinetto, G. Samoggia, and N. Zema, Solid State Commun. **83**, 943 (1992).
[34] V.R. PaiVerneker, A. Petelin, F.J. Crowne, and D.C. Nagle, Phys. Rev. B **40**, 8555 (1989).
[35] H.A. Bethe, *Intermediate Quantum Mechanics* (Benjamin, New York, 1964), Chap. 15.
[36] R.O. Jones and O. Gunnarsson, Rev. Mod. Phys. **61**, 689 (1989).
[37] O. Keski-Rahonen and M.O. Krause, At. Data Nucl. Data Tables **14**, 139 (1974).